Geophysical Research Letters

RESEARCH LETTER
10.1029/2021GL095236

Key Points:

- Time-dependent inversion of InSAR data was performed to infer the co- and post-seismic slip due to the earthquakes along the Chaman fault
- Postseismic/coseismic moment ratios of the M5.5 and M4.7 events are ~0.7 and ~8, both larger than those in many $M > 6$ events
- Long-lasting afterslips appear to overlap with coseismic slip, which may suggest highly heterogeneous friction properties on the fault

Supporting Information:

Supporting Information may be found in the online version of this article.

Correspondence to:

M. Furuya,
furuya@sci.hokudai.ac.jp

Citation:

Furuya, M., & Matsumoto, F. (2022). Post-seismic to co-seismic moment ratios for the 2016 moderate earthquakes along Chaman fault. *Geophysical Research Letters*, *49*, e2021GL095236. https://doi.org/10.1029/2021GL095236

Received 16 JUL 2021
Accepted 17 DEC 2021

Author Contributions:

Conceptualization: Masato Furuya
Data curation: Masato Furuya
Formal analysis: Masato Furuya
Investigation: Masato Furuya, Fumiko Matsumoto
Methodology: Masato Furuya
Project Administration: Masato Furuya
Resources: Masato Furuya
Software: Masato Furuya
Supervision: Masato Furuya
Visualization: Masato Furuya, Fumiko Matsumoto
Writing – original draft: Masato Furuya
Writing – review & editing: Masato Furuya

Post-Seismic to Co-Seismic Moment Ratios for the 2016 Moderate Earthquakes Along Chaman Fault

Masato Furuya[1] and Fumiko Matsumoto[2,3]

[1]Department of Earth and Planetary Sciences, Faculty of Science, Hokkaido University, Sapporo, Japan, [2]Department of Natural History Sciences, Graduate School of Science, Hokkaido University, Sapporo, Japan, [3]Now at PASCO, Tokyo, Japan

Abstract Postseismic-to-coseismic moment ratios (PCMR) for strong ($M > 6$) earthquakes typically do not exceed ~0.3, but there have been limited estimates for moderate-to-small earthquakes. Three M5-class earthquakes and one M4.7 earthquake occurred along the Chaman fault, Pakistan, on May 13 and July 10, 2016. Using Sentinel-1A InSAR time-series from October 2014 to August 2018, we estimate spatial-temporal evolution of the co- and post-seismic fault slip and its velocity. Because of the long-lasting (>1 year) afterslip, the estimated PCMRs of the M5-class events and M4.7 event were 0.7 ± 0.2 and 8.3 ± 2.2, respectively, which are both larger than those of $M > 6$ earthquakes but consistent with previous events that occurred on the Chaman Fault System. Unlike in case of large earthquakes, geodetic inversions are not able to resolve spatial relationships between coseismic slip and afterslip. In case of a non-complementary slip distribution, one explanation might be heterogeneity of friction properties on the fault surface, while other interpretations are possible.

Plain Language Summary An earthquake is a rapid slip on a fault and generates coseismic deformation on the surface. Due to the advent of a radar remote sensing tool called InSAR, we can now map coseismic and postseismic deformation due to slow afterslip on the fault. While the postseismic slip is often much smaller than the coseismic one, particularly for large earthquakes, some reports suggested increasing postseismic slip with decreasing coseismic magnitude, but actual observation data are limited. Here we analyze co- and postseismic deformation due to M5-class earthquakes on a continental strike-slip fault to show that postseismic moment release can be comparable to, or even more significant than the coseismic one. The apparent overlap of co- and postseismic slip distributions might indicate heterogeneous friction properties on the fault surface, while there would be other possible interpretations.

1. Introduction

The Chaman Fault System is a left-lateral transform boundary between the Indian and Eurasian plates (Figure 1a). It is known for its low seismicity, attributed to either a long recurrent interval of large earthquakes or aseismic creep (Ambraseys & Bilham, 2003). Szeliga et al. (2012) detected the secular crustal deformation over the areas mainly from GPS data. They evaluated that 55%–70% of the predicted plate boundary motion accommodated the fault's slip. Recent developments of satellite interferometric synthetic aperture radar (InSAR) have also allowed us to examine the crustal deformation around the fault system. Barnhart (2016) and Fattahi and Amelung (2016) proposed the presence of creeping and locked zones by analyzing spatially much broader and temporally more extended coverage based on Envisat InSAR data.

Meanwhile, Furuya and Satyabala (2008) detected a long-lasting (>1 year) afterslip due to a moment-magnitude (M_w) 5.0 earthquake in 2005 along the Chaman fault, which postseismic/coseismic moment ratio (PCMR) of 5.6 is the largest ever compiled (Alwahedi & Hawthorne, 2019). Furthermore, along the Ghazaband fault that belongs to the Chaman Fault System, Fattahi et al. (2015) also reported a long-lasting afterslip associated with a M_w 5.5 earthquake, whereas the PCMR was ~0.7. We may thus speculate that smaller-magnitude earthquakes could have triggered long-lasting afterslip that accommodates the relative plate motion to the fault slip, which could look like creeping signals in case of infrequent observations. However, to test the hypothesis and examine further details, ground-based geodetic and seismological measurements have been lacking around the Chaman Fault System.

Since the 2005 M_w 5.0 earthquake, no larger earthquakes have indeed occurred along the Chaman fault until May of 2016 (Figure 1b). The United States Geological Survey (USGS) report indicates that the first event on May

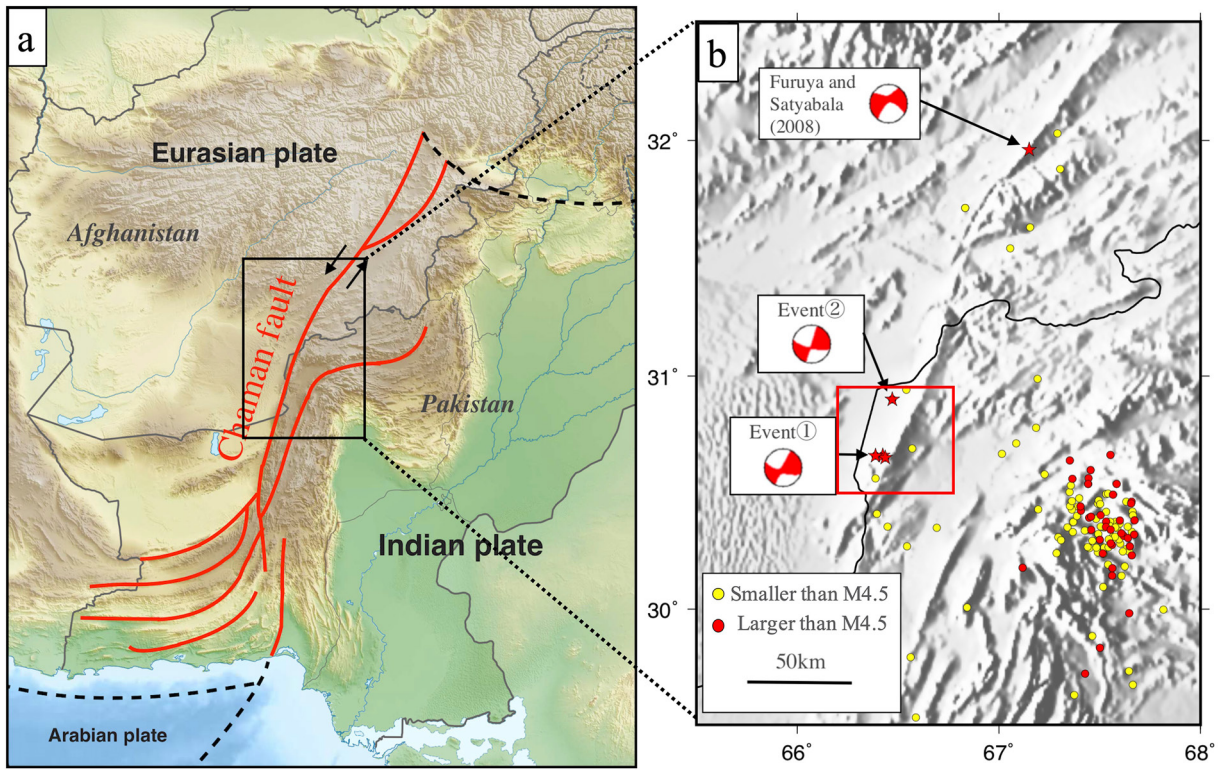

Figure 1. (a) Tectonic setting of the Chaman Fault System. (b) Expanded view of the rectangle in (a) and the nearby earthquakes. Event 1 (M5.2, 4.7, and 5.5) on May 13, 2016 and Event 2 (M4.7) on July 10, 2016 with stars are the target in this study. The locations are determined by United States Geological Survey (USGS). Other circles in red and yellow indicate earthquakes larger or smaller than M4.5, respectively. Also shown is the M5.0 earthquake in 2005 examined by Furuya and Satyabala (2008). The red rectangle corresponds to the analysis area in Figure 3 shown in the Universal Transverse Mercator projection.

13 consists of a triplet with M_w 5.2, 4.7, and 5.5, whereas the second event with body-wave-magnitude (mb) 4.7 occurred on July 10 by ~25 km to the northeast. Hereafter, we call the first M5-class triplet as Event 1 and the later mb 4.7 earthquake as Event 2. As indicated by the use of mb, Event 2 was too small in terms of its seismic moment to determine the moment-magnitude M_w. Notably, the epicenters of both events seem to overlap with the rupture area of the 1892 Chaman earthquake, with estimated M_w ranging from 6.5 to 6.7 (Bilham et al., 2019).

The PCMR estimates for large ($M > 6$) earthquakes are roughly around 0.3 or less and have no systematic trend with coseismic magnitude (Alwahedi & Hawthorne, 2019). This is consistent with a self-similar model of earthquakes based on the assumption of constant stress drop over a wide range of seismic moments (e.g., Abercrombie, 1995). Toward the limit of smaller earthquakes, however, the self-similar model has been contentious. In particular, from a rich record of repeating earthquakes along the Parkfield segment of the San Andreas Fault, Nadeau and Johnson (1998) suggested that stress drop increases with decreasing seismic moment; similar relationships have been confirmed from repeating earthquakes in different tectonic settings (Chen et al., 2007; Igarashi et al., 2003). On the theoretical side, Chen and Lapusta (2009) simulated repeating earthquakes based on the rate-and-state friction (RSF) law (Dieterich, 2007), suggesting that aseismic slip may increase with decreasing coseismic magnitude. However, the PCMR for moderate to smaller earthquakes is not well-constrained. Estimating the spatial and temporal distribution of fault slip and constraining the PCMR have implications for possible size-dependence in the dynamics of earthquakes and frictional properties of faults (Alwahedi & Hawthorne, 2019). The 2016 moderate earthquakes along the Chaman fault provide us with an excellent opportunity to examine the PCMR.

Using the Sentinel-1 InSAR data sets from 2014 to 2018, we perform a time-dependent fault slip and slip velocity inversion based on Kalman filter that has been developed for geodetic time-series data (e.g., Bartlow et al., 2014; Bekaert et al., 2016; Miyazaki et al., 2004, 2006; Segall & Matthews, 1997; Segall et al., 2000; Shirzaei & Bürgmann, 2013; Xue et al., 2020). In contrast to the complementary location of afterslip to coseismic slip in $M > 6$

earthquakes, our inversions are not able to resolve details of relative location of afterslip and coseismic slip. We discuss the nonuniqueness of the slip estimates and its implication for the inversion procedure, and speculate on possible mechanisms of complementary and non-complementary distributions of co- and post-seismic slip.

2. Materials and Methods

2.1. InSAR Time-Series Data

We use European Space Agency's Sentinel-1A Interferometric Wide swath mode 75 SAR images from October 2014 to August 2018 to generate 428 interferograms in total, using a commercial software package by Gamma remote sensing (Wegmüller & Werner, 1997). Topographic phases are corrected using the 30m mesh Digital Elevation Model by Shuttle Radar Topography Mission (Farr et al., 2007). We perform small-baseline subset (SBAS)-type time-series analysis (e.g., Berardino et al., 2002; Schmidt & Bürgmann, 2003), using the LiCSBAS package by Morishita et al. (2020), over the clipped 50×50 km^2 region (Figure 1); see Supporting Information S1 for further details. Because the first SAR imaging after Event 1 and 2 was done by 5 and 19 days after each event, we, unfortunately, missed the earlier slip evolutions, particularly for Event 2. We thus use the seismological coseismic moment estimates by USGS to compute the PCMR for each event; we summed up each moment of the triplet in Event 1. Our previous studies indicate that both seismological and InSAR-based estimates of the coseismic moment are mostly consistent (e.g., Furuya & Yasuda, 2011; Himematsu & Furuya, 2016).

2.2. Time-Dependent Fault Modeling

Our time-dependent inversion follows the linear Kalman filtering (LKF) by Bekaert et al. (2016), but there are a few differences. As we removed a planar ramp in deriving the InSAR time series, no long-wavelength secular deformation signals are left, and we do not estimate plate motion velocity. Unlike Bartlow et al. (2011) and Bekaert et al. (2016), we do not apply the non-negativity constraint on both slip and slip velocity. As noted below, we set non-zero slip and velocity as the initial values to estimate the afterslip, which would be already a significant constraint. Moreover, as LKF is incapable of estimating temporally sudden changes such as coseismic slip, we separately perform the modeling before and after Event 1; we set zero initial values for the period before Event 1. To evaluate the afterslip for Event 1 and 2, we provide coseismic slip for both Event 1 and 2 as the initial values in the Kalman filter, which we estimated by a conventional damped least squares inversion (e.g., Furuya & Yasuda, 2011; Himematsu & Furuya, 2016). The epoch-by-epoch least squares solutions were helpful to infer the variance-covariance matrix for InSAR observation uncertainties (Figure S1 in Supporting Information S1). Initial slip velocities are also necessary, which we derived so that the product of the slip velocity and the time interval could become consistent with the cumulative slip. We set the initial uncertainties in the state vector to be 0.5 cm slip and 10^{-8} cm/day slip velocity as in Bekaert et al. (2016).

In the time-dependent slip inversion based on the Kalman filter, two hyperparameters control data fitting and the smoothness in spatial slip distribution and temporal slip evolution. We perform a grid-search over a range of hyperparameters to narrow down the "optimum" hyper-parameters, running the LKF from the first post-earthquake epoch to February 13, 2018, to save computation time. Following Miyazaki et al. (2006), we examine the objective function, $\Phi(s) = \|d - Gs\|^2 + \lambda^2 (\|\nabla^2 s\|^2 + \|\nabla 2\dot{s}\|^2) + \alpha^2 (\|s\|^2 + \|\dot{s}\|^2)$; d is data, s is slip, G is a Green function of elastostatic deformation, and λ and α are the hyperparameters which weight the smoothness and minimum norm constraints. Shown in Figures 2a–2c are the squared misfit residuals $\|d - Gs\|^2$, smoothness $\|\nabla^2 s\|^2 + \|\nabla 2\dot{s}\|^2$ and norm $\|s\|^2 + \|\dot{s}\|^2$ as a function of the two parameters. We see an apparent trade-off between the misfit, solution roughness, and norm. As was the case in Bartlow et al. (2014), Figure 2d indicates that there is no clear "minimum." We thus set $\alpha = 10^{-5}$ and $\lambda = 10^{-2}$ as our preferred hyperparameters and visually checked that the results were essentially the same, whatever the nearby hyperparameters were used. We use the same hyperparameters for the pre-earthquake InSAR time series.

3. Results

Figure 3 shows the selected six sequences of the observed, calculated LOS changes, and their misfit residuals at the indicated epochs in days after Event 1/2; Figure S2 in Supporting Information S1 shows results for other epochs. The spatial pattern of the LOS changes after the Event 1 is consistent with the left-lateral strike-slip motion

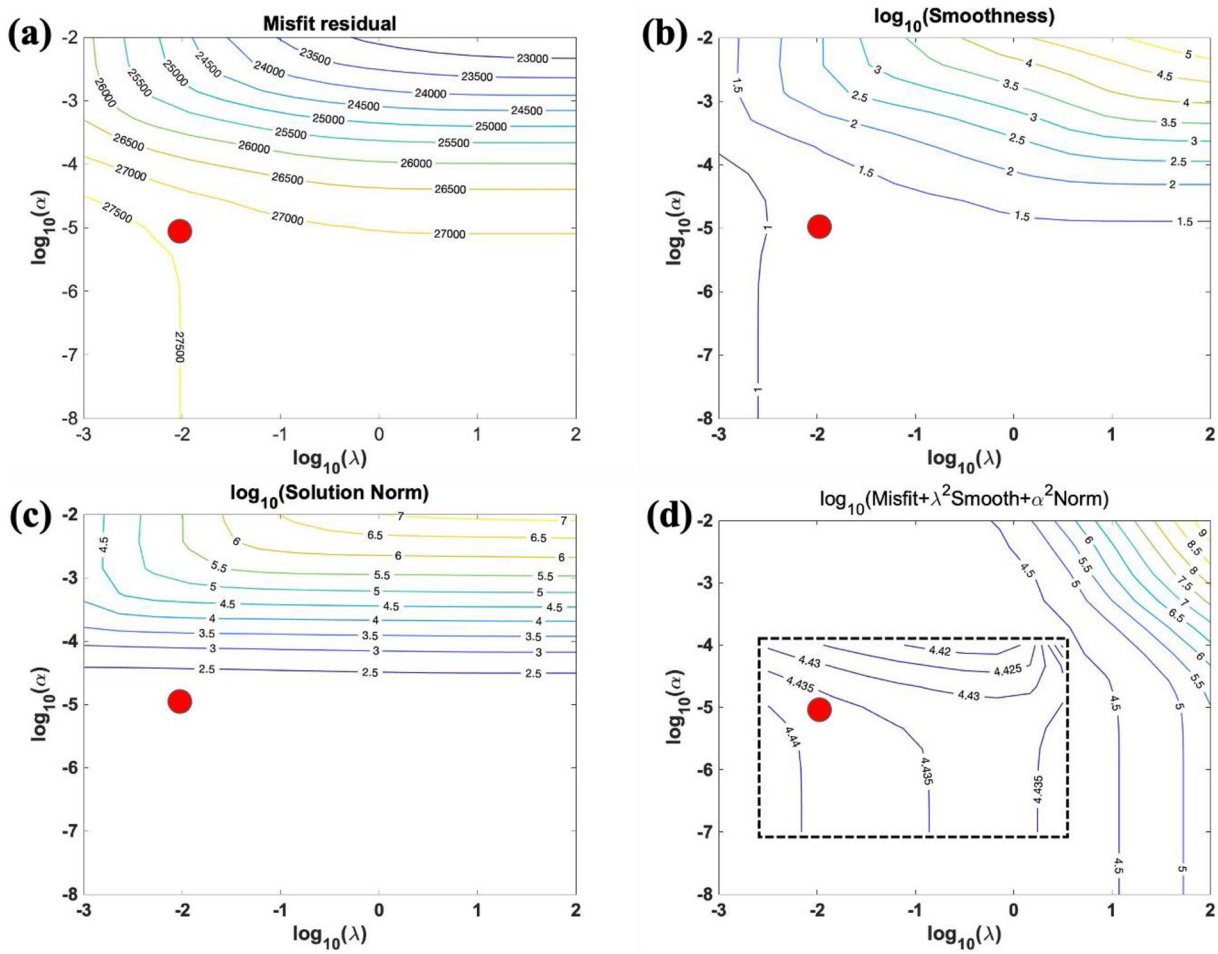

Figure 2. Trade-off effects of the two hyperparameters on the (a) misfit residual, (b) solution smoothness, and (c) norm over the prescribed range values. Shown with a dashed square in (d) is our detailed search with the narrowed hyperparameters. The red circle indicates our preferred parameters in this study.

in the near-vertical fault of Event 1 and 2. The amplitude increase and expansion of the LOS change over time by Event 1 and 2 are apparent in the earlier stage near the epicenter. Also, we notice that the LOS changes by Event 2 are discontinuous across the Chaman fault, which is not the case in Event 1.

Figure 4 shows the estimated cumulative slip and slip velocity at each epoch at the same six epochs in Figure 3**;** see Figures S3 in Supporting Information S1 for other epochs and formal errors. Although nearly all the estimates at any depths in Figure 4 are well beyond the formal errors (Figures S3 in Supporting Information S1), we regard those estimates near the bottom and edges as artifacts. The pre-earthquake estimates in Figures 4a and 4g clearly illustrate artifacts, presumably derived from accounting for the broadly distributed uncorrected tropospheric delays despite the absence of evident LOS changes across the fault (Figure 3a); see also Figure S2 in Supporting Information S1. The broader the LOS change signals, the deeper and larger slips are estimated. As evident from the estimates after the earthquake (Figure 4), artifact slips will accumulate over time. On the contrary, we regard the persistently appearing estimates at shallower depths as genuine fault slip and slip velocity.

At earlier epochs, the slip areas are essentially circular in both Event 1 and 2, around the depths of ~7 and 3 km, respectively. Although the afterslip of Event 2 reaches the surface, that of Event 1 does not; we have confirmed by plotting the slip distribution with a logarithmic scale, and the slip reached 3–4 cm. The rupture to the surface by Event 2 is responsible for the discontinuous LOS changes across the fault. Also, there exist apparent slip gaps between Event 1 and 2. If we roughly evaluate the slip gap areas as 30 × 10 km and assume an average slip of 0.5–1.0 m, the corresponding earthquake magnitude would be M_w 6.4–6.6, consistent with the 1892 event and suggests that they were the slipped area in 1892.

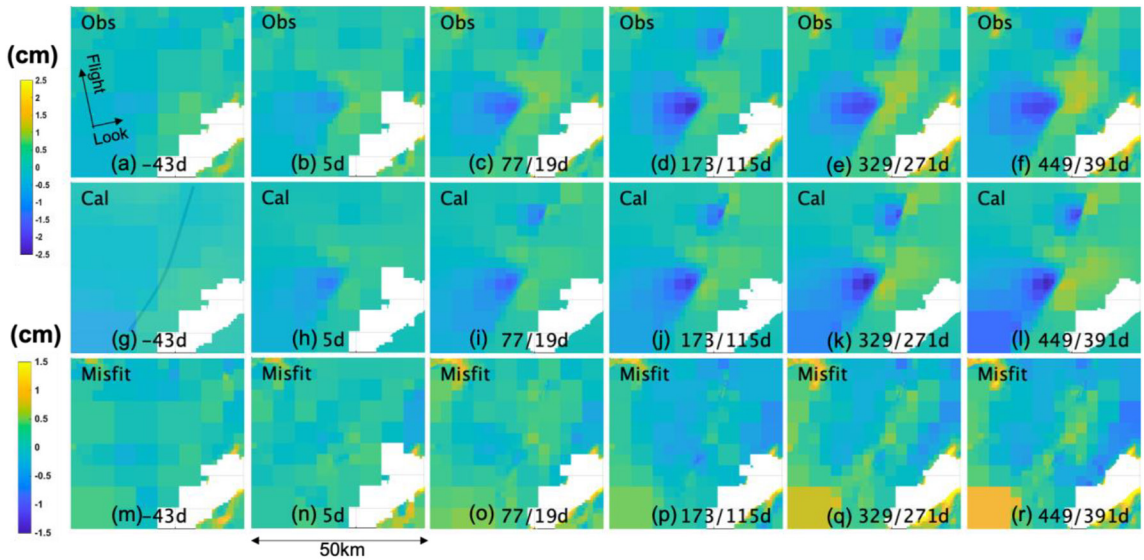

Figure 3. Selected sequences of the observed (a–f), calculated (g–l) LOS changes, and their misfit residuals (m–r). The bottom of each panel is the number of days after Event 1 on May 13, 2016, and Event 2 on July 10, 2016. Satellite flight and radar illuminating direction are shown in (a). The location of the fault model is shown in (g).

Based on the moment release evolution in Figure 5, we estimate the PCMR as of 2017.5 are 0.7 ± 0.2 and 8.3 ± 2.2 for Event 1 and 2, respectively. The two PCMR estimates appear significantly different from each other. However, comparing with the previous estimates around Chaman Fault System, the PCMR for Event 1 is the same as that on the 2007 Ghazaband M_w 5.5 earthquake (Fattahi et al., 2015), and that for Event 2 is even larger than the estimate (5.6) on the 2005 M_w 5.0 earthquake by Furuya and Satyabala (2008). The PCMR of 0.7 for Event 1 may appear small but is still significant, compared with other $M > 6$ earthquakes (Alwahedi & Hawthorne, 2019; Fattahi et al., 2015).

In both Event 1 and 2, Figure 5 indicates that the moment release rates were higher during the earlier period, while Figure 4 tell that the afterslip lasted more than one year. Although we can observe, to some extent, an expansion of the slip area both laterally and toward shallower depth, the increasing cumulative slip amplitude is essential to generate the large PCMR. Inspecting Figure 4 in detail, we notice that the slip patches with faster slip velocity do not quickly slow down but keep slipping for more than one year while outer patches are slowing down (Figure 4). Moreover, those fastest slip patches stay inside the coseismic ones where the earthquakes nucleated (Figures 4k and 4l). The triangular mesh size is less than 2.5 km at a depth of about 5 km, where the most significant slip was detected. Considering that a uniform slip of 0.3 m over 3.0 × 1.5 km^2 area gives M_w 5, we may conclude that the largest co- and postseismic slip patches are noncomplementary. We should keep in mind, however, that the inferred slip distribution is not unique as discussed later.

The maximum afterslip velocities of Event 1 and 2 depend on the coseismic magnitude, whereas coseismic slip velocities are known to be constant over a wide range of earthquake magnitude. Slip velocities during the early stage after Event 1 and 2 are on the order of 6×10^{-4} m/d and 3×10^{-4} m/d, respectively. The 2005 M_w 5.0 event also reveals slip velocities on the order of 10^{-4} m/d or less in the beginning period (Furuya & Satyabala, 2008).

4. Discussion and Conclusion

RSF law can explain a variety of processes during the earthquake cycle, including initiation of an earthquake, subsequent development of coseismic**,** postseismic afterslip, and interseismic slip on a fault, by the spatial variations of steady rate-and-state parameters $a-b$ on fault (e.g., Dieterich, 2007; Scholz, 1998). A velocity weakening (VW) region with negative $a-b$ loses frictional strength with increasing slip velocity and is potentially seismogenic. For the slip to grow as an earthquake, the VW region needs to be greater than a critical nucleation size (Chen & Lapusta, 2009; Rubin & Ampuero, 2005). On the other hand, a velocity strengthening (VS) region with positive $a-b$ gains its strength with increasing slip velocity, surrounding VW region, and hosts stable aseismic

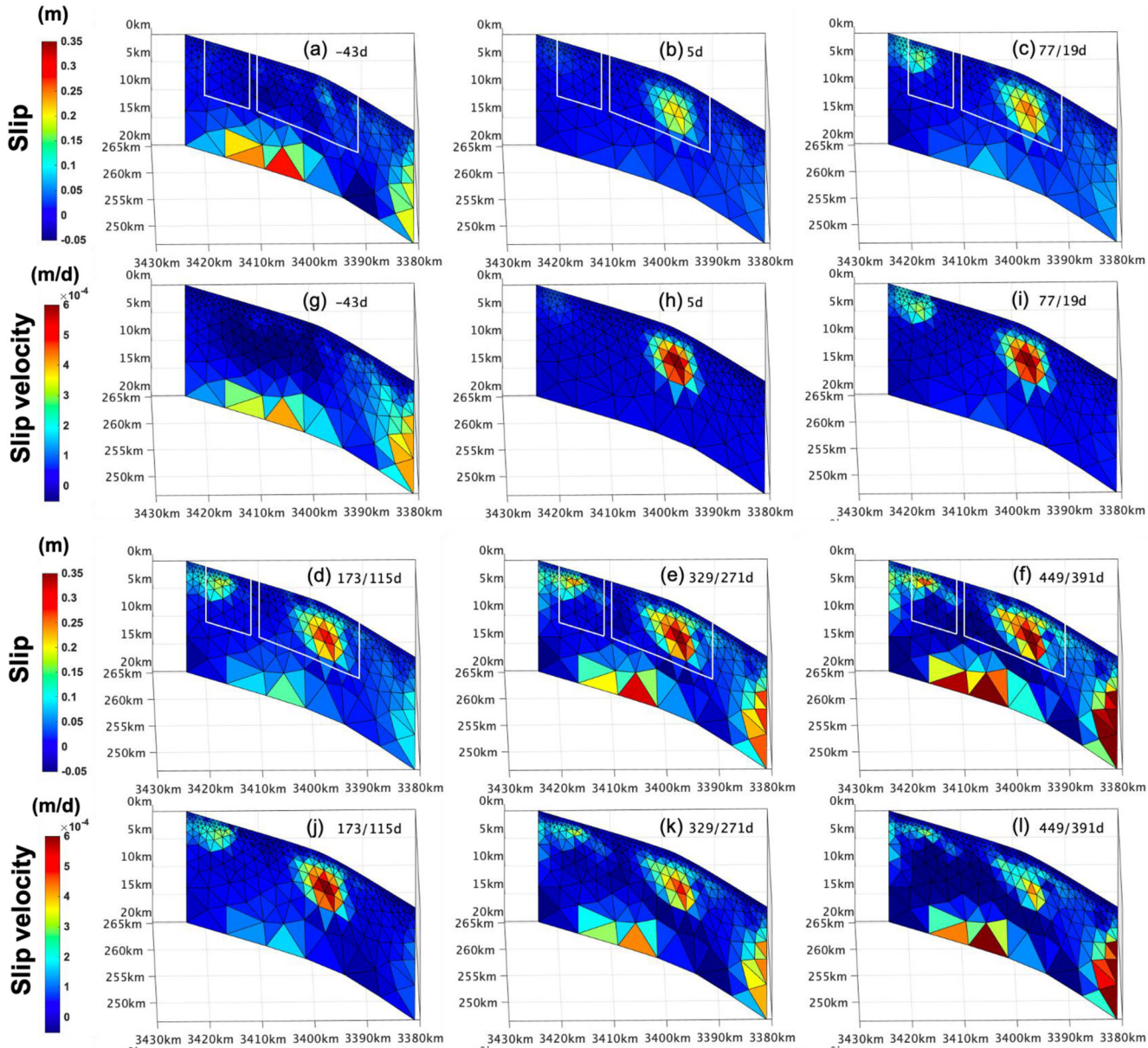

Figure 4. Selected snapshots for the estimated slip (a–c, d–f first, and third rows) and slip velocity (g–i, j–l second, and fourth rows). Numbers in the upper right of each panel are the elapsed days before and after Event 1 on May 13, 2016, and Event 2 on July 10, 2016. We performed time-dependent inversion separately before and after the earthquakes. Therefore, slip estimates from (b), (c), and (d) to (f) are cumulative ones. We include the slip values inside the two white rectangles in the first and third rows for moment release calculation. See Figure 3g for the location and geometry of the fault model.

slip during both interseismic and postseismic stages. Spatial distribution of coseismic slip and postseismic afterslip has been demonstrated to be complementary by, for instance, Miyazaki et al. (2004) for the 2003 M8.0 Tokachi-Oki earthquake, Hsu et al. (2006) for the 2005 M8.7 Nias-Simeulue earthquake, and Barbot et al. (2009) for the 2004 M6.0 Parkfield earthquake.

In contrast, the postseismic afterslip of both Event 1 and 2 most significantly took place near the center of the slip patches and lasted more than a year. The co-location of co- and post-seismic slip is different from the spatial distribution of the afterslip by $M > 6$ earthquakes but is consistent with our previous report (Furuya & Satyabala, 2008). Fattahi et al. (2015) also reported the significant overlap of co- and post-seismic slip patches in the M_w 5.5 Ghazaband earthquake in the Chaman Fault System. Moreover, long-lived slip velocity patches are estimated

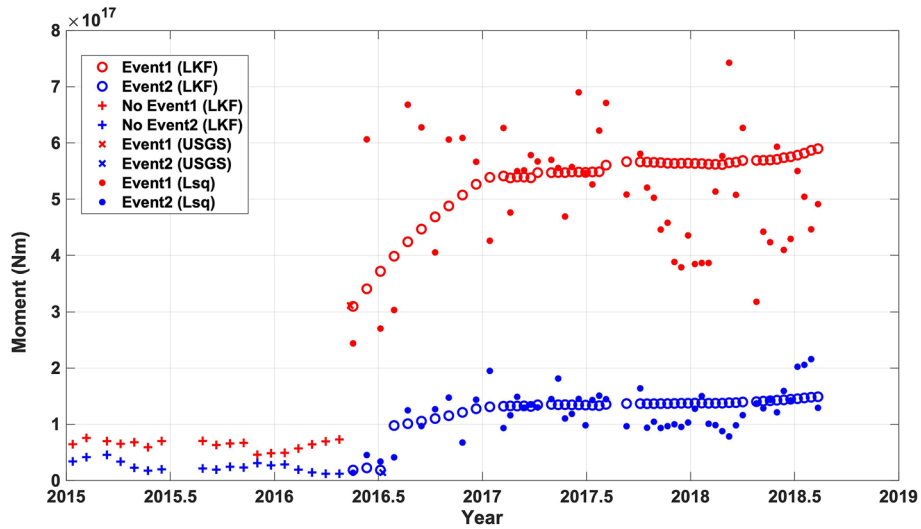

Figure 5. Cumulative moment release for Event1 (red circle, linear Kalman filtering (LKF)) and Event 2 (blue circle, LKF) calculated from the estimated slip patches inside the white lines in Figure 4. Also shown are the estimated moment release from the same LKF from the pre-earthquake data (red and blue plus signs, LKF) and the epoch-by-epoch damped least squares (asterisks, Lsq). Seismological coseismic moment estimates for Event 1 and 2 by United States Geological Survey are shown with red and blue crosses, respectively.

near the center (Figure 4), which is in conflict with the complementary slip evolution inferred in larger ($M > 6$) earthquakes.

The inferred slip distributions are, however, not unique. We performed simple synthetic experiments to show the other possible solutions. At the 4 epochs (c, d, e, and f) in Figure 3, we modified the slip amplitude near the center of the patches close to the co-seismic values and made the slip amplitude in the surrounding patches larger by a factor of 1.2–1.3, so that the co- and post-seismic slip distributions can appear complementary; VW region is surrounded by VS region. Figures S4–S7 in Supporting Information S1 show not only consistent moment release but also a surface deformation map that is indistinguishable from the original calculated one. These synthetic experiments, however, do demonstrate that complementary co- and post-seismic slip distributions cannot be resolved in the present size of earthquakes unless we impose an additional constraint on how the slip and velocity should distribute on the fault surface. Moreover, even if the complementary co- and postseismic slip distributions are consistent with those in the previous large earthquakes, it is still uncertain if RSF law can reasonably account for the large PCMR and the long duration of afterslip with the $a-b$ distribution noted above.

It is difficult to interpret the inferred noncomplementary co- and post-seismic slip distributions as they are, using the RSF law, because steady rate-and-state parameters $a-b$ for the VW region are assumed to be negative over a range of slip velocities. Namely, if the VW region is significantly larger than a critical nucleation size, the entire VW region will undergo seismic slip that is only stopped by the surrounding VS region. Thus no postseismic afterslip can be expected inside the VW region (e.g., Chen & Lapusta, 2009) as demonstrated in the studies of $M > 6$ earthquakes (e.g., Lindsey & Fialko, 2016). However, it is possible to regard the noncomplementary co- and postseismic slip distributions as apparent ones that were derived due to the lack of resolution. Namely, if the friction parameters are heterogeneously distributed with characteristic spacings on the order of km-to sub-km-scale (Furuya & Satyabala, 2008; Jiang & Fialko, 2016; Shaddox et al., 2021), we may expect both moderate earthquakes and long-lasting afterslip on the same patch with a scale greater than km. Although we have modeled as a single event, the three earthquakes of Event 1 may possibly correspond to three individual VW regions that could not be resolved in this study. Jiang and Fialko (2016) explicitly considered heterogenous friction parameters on a fault surface in their numerical model, aiming to account for the apparent inconsistency between the seismicity and geodetically inferred locking depth at Anza section of the San Jacinto Fault. Similar forward modeling is necessary not only to reproduce the observed long-lasting afterslip but also to understand the present status of the ruptured area in 1892.

We also note that some experimental and theoretical studies (e.g., Bar-Sinai et al., 2014; Kaproth & Marone, 2013; Shimamoto, 1986) have indicated a transition of the $a-b$ from negative (VW) to positive (VS) with increasing slip velocities. The transition effect from VW to VS with a cutoff slip velocity can generate slow but faster slip than plate motion velocity and has been incorporated in many simulations of slow slip events (SSE, e.g., Hawthorne & Rubin, 2013; Im et al., 2020; Matsuzawa et al., 2010; Shibazaki & Iio, 2003), but the occurrence of regular earthquakes is prohibited. However, if there were an enhanced VW before transition to VS, it could generate both small to moderate regular earthquakes and afterslip, which may be dubbed as nonsilent SSE. Although the idea is speculative, some experimental data show a complicated dependence of the friction on sliding velocity (e.g., Bar-Sinai et al., 2014), and it would be another possible scenario. Further experimental and theoretical validations are needed.

We can conceive other possible processes by changes in the effective normal stress without tuning frictional parameters in RSF law. Dynamic ruptures on fault will generate tensile microcracks, reduce pore fluid pressure near the fault, and enhance effective normal stress. Meanwhile, frictional heating following the dynamic rupture can also raise the pore fluid pressure on the fault and thus will reduce effective normal stress (e.g., Segall et al., 2010; Suzuki & Yamashita, 2009). Although these theoretical studies aim to understand the mechanism of SSEs in subduction zones, we may expect similar processes in continental faults. However, it is uncertain if and how pore fluids can be supplied in the shallow continental faults, and further observational and experimental studies are necessary.

Data Availability Statement

The original Sentinel-1 SAR data are freely available from Copernicus Open Access Hub https://scihub.copernicus.eu/dhus, whereas user registration is needed. We used IW-mode SLC data along the ascending track 42. Each granule name is listed in Table S1 in Supporting Information S1. InSAR time-series data from LiCSBAS are saved as HDF files, which are available at https://doi.org/10.5281/zenodo.4381296. Those HDF files were imported in MATLAB to perform the time-dependent inversion. The MATLAB M-files are available at https://doi.org/10.5281/zenodo.5635536.

Acknowledgments
The authors thank Bun'ichiro Shibazaki for the discussion on the mechanisms of our observations. The authors also acknowledge two anonymous reviewers whose comments were constructive and helpful to improve the original manuscript.

References

Abercrombie, R. E. (1995). Earthquake source scaling relationships from −1 to 5 ML using seismograms recorded at 2.5-km depth. *Journal of Geophysical Research*, *100*(B12), 24015–24036. https://doi.org/10.1029/95JB02397

Alwahedi, M. A., & Hawthorne, J. C. (2019). Intermediate-magnitude postseismic slip follows intermediate-magnitude (M 4 to 5) earthquakes in California. *Geophysical Research Letters*, *46*, 3676–3687. https://doi.org/10.1029/2018GL081001

Ambraseys, N., & Bilham, R. (2003). Earthquakes in Afghanistan. *Seismological Research Letters*, *74*(2), 107–23. https://doi.org/10.1785/gssrl.74.2.107

Barbot, S., Fialko, Y., & Bock, Y. (2009). Postseismic deformation due to the Mw 6.0 2004 Parkfield earthquake: Stress-driven creep on a fault with spatially variable rate-and-state friction parameters. *Journal of Geophysical Research*, *114*, B07405. https://doi.org/10.1029/2008JB005748

Barnhart, W. D. (2016). Fault creep rates of the Chaman fault (Afghanistan and Pakistan) inferred from InSAR. *Journal of Geophysical Research: Solid Earth*. https://doi.org/10.1002/2016JB013656

Bar-Sinai, Y., Spatschek, R., Brener, E. A., & Bouchbinder, E. (2014). On the velocity-strengthening behavior of dry friction. *Journal of Geophysical Research: Solid Earth*, *119*, 1738–1748. https://doi.org/10.1002/2013JB010586

Bartlow, N. M., Miyazaki, S., Bradley, A. M., & Segall, P. (2011). Space-time correlation of slip and tremor during the 2009 Cascadia slow slip event. *Geophysical Research Letters*, *38*, L18309. https://doi.org/10.1029/2011GL048714

Bartlow, N. M., Wallace, L. M., Beavan, R. J., Bannister, S., & Segall, P. (2014). Time-dependent modeling of slow slip events and associated seismicity and tremor at the Hikurangi subduction zone, New Zealand. *Journal of Geophysical Research: Solid Earth*, *119*(1), 734–753. https://doi.org/10.1002/2013JB010609

Bekaert, D. P. S., Segall, P., Wright, T. J., & Hooper, A. J. (2016). A network inversion filter combining GNSS and InSAR for tectonic slip modeling. *Journal of Geophysical Research: Solid Earth*, *121*(3), 2069–2086. https://doi.org/10.1002/2015JB012638

Berardino, P., Fornaro, G., Lanari, R., & Sansosti, E. (2002). A new algorithm for surface deformation monitoring based on small baseline differential SAR interferograms. *IEEE Transactions on Geoscience and Remote Sensing*, *40*(11), 2375–2383. https://doi.org/10.1109/TGRS.2002.803792

Bilham, R., Kakar, N. U., Kakar, D. M., Wang, K., Bürgmann, R., & Barnhart, W. D. (2019). The 1892 chaman, Pakistan, earthquake. *Seismological Research Letters*, *90*(6), 2293–2303. https://doi.org/10.1785/0220190148

Chen, K. H., Nadeau, R. M., & Rau, R.-J. (2007). Towards a universal rule on the recurrence interval scaling of repeating earthquakes? *Geophysical Research Letters*, *34*, L16308. https://doi.org/10.1029/2007GL030554

Chen, T., & Lapusta, N. (2009). Scaling of small repeating earthquakes explained by interaction of seismic and aseismic slip in a rate and state fault model. *Journal of Geophysical Research*, *114*, B01311. https://doi.org/10.1029/2008JB005749

Dieterich, J. H. (2007). Applications of rate- and state-dependent friction to models of fault slip and earthquake occurrence. In G. Schubert (Ed.), *Treatise on geophysics* (Vol. 4, pp. 107–129). Elsevier. https://doi.org/10.1016/B978-044452748-6.00065-1

Farr, T. G., & Kobrick, M. (2007). The shuttle radar topography mission. *Review of Geophysics*, *45*, RG2004. https://doi.org/10.1029/2005RG000183

Fattahi, H., & Amelung, F. (2016). InSAR observations of strain accumulation and fault creep along the Chaman Fault system, Pakistan and Afghanistan. *Geophysical Research Letters*. https://doi.org/10.1002/2016GL070121

Fattahi, H., Amelung, F., Chaussard, E., & Wdowinski, S. (2015). Coseismic and postseismic deformation due to the 2007 M5.5 Ghazaband fault earthquake, Balochistan, Pakistan. *Geophysical Research Letters*, *42*, 3305–3312. https://doi.org/10.1002/2015GL063686

Furuya, M., & Satyabala, S. P. (2008). Slow earthquake in Afghanistan detected by InSAR. *Geophysical Research Letters*, *35*, L06309. https://doi.org/10.1029/2007GL033049

Furuya, M., & Yasuda, T. (2011). The 2008 Yutian normal faulting earthquake (Mw 7.1), NW Tibet: Non-planar fault modeling and implications for the Karakax Fault. *Tectonophysics*, *511*(3–4), 125–133. https://doi.org/10.1016/j.tecto.2011.09.003

Hawthorne, J. C., & Rubin, A. M. (2013). Laterally propagating slow slip events in a rate and state friction model with a velocity-weakening to velocity-strengthening transition. *Journal of Geophysical Research: Solid Earth*, *118*, 3785–3808. https://doi.org/10.1002/jgrb.50261

Himematsu, Y., & Furuya, M. (2016). Fault source model for the 2016 kumamoto earthquake sequence based on ALOS-2/PALSAR-2 pixel-offset data: Evidence for dynamic slip partitioning. *Earth Planets and Space*, *68*(1), 169. https://doi.org/10.1186/s40623-016-0545-7

Hsu, Y.-J., Simons, M., Avouac, J.-P., Galtezka, J., Sieh, K., Chlieh, M., et al. (2006). Frictional afterslip following the 2005 Nias-Simeulue earthquake, Sumatra. *Science*, *312*, 1921–1926. https://doi.org/10.1126/science.1126960

Igarashi, T., Matsuzawa, T., & Hasegawa, A. (2003). Repeating earthquakes and interplate aseismic slip in the northeastern Japan subduction zone. *Journal of Geophysical Research*, *108*(B5), 2249. https://doi.org/10.1029/2002JB001920

Im, K., Saffer, D., Marone, C., & Avouac, J. P. (2020). Slip-rate-dependent friction as a universal mechanism for slow slip events. *Nature Geoscience*, *13*, 705–710. https://doi.org/10.1038/s41561-020-0627-9

Jiang, J., & Fialko, Y. (2016). Reconciling seismicity and geodetic locking depths on the Anza section of the San Jacinto fault. *Geophysical Research Letters*, *43*, 10663–10671. https://doi.org/10.1002/2016GL071113

Kaproth, B. M., & Marone, C. (2013). Slow earthquakes, preseismic velocity changes, and the origin of slow frictional Stick-slip. *Science*, *341*, 1229–1232. https://doi.org/10.1126/science.1239577

Lindsey, E. O., & Fialko, Y. (2016). Geodetic constraints on frictional properties and earthquake hazard in the Imperial Valley, Southern California. *Journal of Geophysical Research: Solid Earth*, *121*, 1097–1113. https://doi.org/10.1002/2015JB012516

Matsuzawa, T., Hirose, H., Shibazaki, B., & Obara, K. (2010). Modeling short- and long-term slow slip events in the seismic cycles of large subduction earthquakes. *Journal of Geophysical Research*, *115*, B12301. https://doi.org/10.1029/2010JB007566

Miyazaki, S., Segall, P., Fukuda, J., & Kato, T. (2004). Space time distribution of afterslip following the 2003 Tokachi-oki earthquake: Implications for variations in fault zone frictional properties. *Geophysical Research Letters*, *31*, L06623. https://doi.org/10.1029/2003GL019410

Miyazaki, S., Segall, P., McGuire, J. J., Kato, T., & Hatanaka, Y. (2006). Spatial and temporal evolution of stress and sliprate during the 2000 Tokai slow earthquake. *Journal of Geophysical Research*, *111*, B03409. https://doi.org/10.1029/2004JB003426

Morishita, Y., Lazecky, M., Wright, T. J., Weiss, J. R., Elliott, J. R., & Hooper, A. (2020). LiCSBAS: An open-source InSAR time series analysis package integrated with the LiCSAR automated Sentinel-1 InSAR processor. *Remote Sensing*, *12*, 424. https://doi.org/10.3390/RS12030424

Nadeau, R. M., & Johnson, L. R. (1998). Seismological studies at Park- field VI: Moment release rates and estimates of source parameters for small repeating earthquakes. *Bulletin of the Seismological Society of America*, *88*, 790–814. https://doi.org/10.1785/BSSA0880030790

Rubin, A. M., & Ampuero, J.-P. (2005). Earthquake nucleation on (aging) rate and state faults. *Journal of Geophysical Research*, *110*, B11312. https://doi.org/10.1029/2005JB003686

Schmidt, D. A., & Bürgmann, R. (2003). Time-dependent land uplift and subsidence in the Santa Clara valley, California, from a large interferometric synthetic aperture radar data set. *Journal of Geophysical Research*, *108*(B9), 2416. https://doi.org/10.1029/2002JB002267

Scholz, C. (1998). Earthquakes and friction laws. *Nature*, *391*, 37–42. https://doi.org/10.1038/34097

Segall, P., Bürgmann, R., & Matthews, M. (2000). Time dependent triggered afterslip following the 1989 Loma Prieta earthquake. *Journal of Geophysical Research*, *105*, 5615–5634. https://doi.org/10.1029/1999JB900352

Segall, P., & Matthews, M. (1997). Time dependent inversion of geodetic data. *Journal of Geophysical Research*, *102*(B10), 22391–22409. https://doi.org/10.1029/97JB01795

Segall, P., Rubin, A. M., Bradley, A. M., & Rice, J. R. (2010). Dilatant strengthening as a mechanism for slow slip events. *Journal of Geophysical Research*, *115*, B12305. https://doi.org/10.1029/2010JB007449

Shaddox, H. R., Schwartz, S. Y., & Bartlow, N. M. (2021). Afterslip and spontaneous aseismic slip on the Anza segment of the San Jacinto fault zone, Southern California. *Journal of Geophysical Research: Solid Earth*, *126*, e2020JB020460. https://doi.org/10.1029/2020JB020460

Shibazaki, B., & Iio, Y. (2003). On the physical mechanism of silent slip events along the deeper part of the seismogenic zone. *Geophysical Research Letters*, *30*(9), 1489. https://doi.org/10.1029/2003GL017047

Shimamoto, T. (1986). Transition between frictional slip and ductile flow for halite shear zones at room temperature. *Science*, *231*, 711–714. https://doi.org/10.1126/science.231.4739.711

Shirzaei, M., & Bürgmann, R. (2013). Time-dependent model of creep on the Hayward fault from joint inversion of 18 years of InSAR and surface creep data. *Journal of Geophysical Research: Solid Earth*, *118*(4), 1733–1746. https://doi.org/10.1002/jgrb.50149

Suzuki, T., & Yamashita, T. (2009). Dynamic modeling of slow earthquakes based on thermoporoelastic effects and inelastic generation of pores. *Journal of Geophysical Research*, *114*, B00A04. https://doi.org/10.1029/2008JB006042

Szeliga, W., Bilham, R., Kakar, D. M., & Lodi, S. H. (2012). Interseimic strain accumulation along the western boundary of the Indian subcontinent. *Journal of Geophysical Research*, *117*, B08404. https://doi.org/10.1029/2011JB008822

Wegmüller, U., & Werner, C. L. (1997). Gamma SAR processor and interferometry software. In *Procceedings of the 3rd ERS symposium* (pp. 1687–1692). European Space Agency Special Publication. (ESA SP-414).

Xue, X., Freymueller, J., & Lu, Z. (2020). Modeling the posteruptive deformation at Okmok based on the GPS and InSAR time series: Changes in the shallow magma storage system. *Journal of Geophysical Research: Solid Earth*, *125*, e2019JB017801. https://doi.org/10.1029/2019JB017801

References From the Supporting Information

Comninou, M., & Dunders, J. (1975). The angular dislocation in a half space. *Journal of Elasticity*, *5*, 203–216.

Geuzaine, C., & Remacle, J. F. (2009). Gmsh: A 3-D finite element mesh generator with built-in pre- and post-processing facilities. *International Journal for Numerical Methods in Engineering*, *79*(11), 1309–1331.

Hanssen, R. F. (2001). *Radar interferometry: Data interpretation and error analysis*. Kluwer Academic Press.

Jolivet, R., Agram, P. S., Lin, N. Y., Simons, M., Doin, M.-P., Peltzer, G., & Li, Z. (2014). Improving InSAR geodesy using global atmospheric models. *Journal of Geophysical Research: Solid Earth*, *119*, 2324–2341. https://doi.org/10.1002/2013JB010588

Jónsson, S., Zebker, H., Segall, P., & Amelung, F. (2002). fault slip distribution of the 1999 Mw 7.1 hector mine, California, earthquake, estimated from satellite radar and GPS measurements. *Bulletin of the Seismological Society of America*, *92*(4), 1377–1389.

Kinoshita, Y., Furuya, M., & HobigerIchikawa, T. R. (2013). Are numerical weather model outputs helpful to reduce tropospheric delay signals in InSAR data? *Journal of Geodesy*, *87*(3), 267–277. https://doi.org/10.1007/s00190-012-0596-x

Lohman, R. B., & Simons, M. (2005). Some thoughts on the use of InSAR data to constrain models of surface deformation: Noise structure and data downsampling. *Geochemistry, Geophysics, Geosystems*, *6*, Q01007. https://doi.org/10.1029/2004GC000841

Meade, B. J. (2007). Algorithms for the calculation of exact displacements, strains, and stresses for triangular dislocation elements in a uniform elastic half space. *Computers and Geosciences*, *33*, 1064–1075. https://doi.org/10.1016/j.cageo.2006.12.003

Nur, A., & Mavko, G. (1974). Postseismic viscoelastic rebound. *Science*, *183*(4121), 204–206.

Yoffe, E. (1960). The angular dislocation. *Philosophical Magazine*, *5*, 161–175.

Yu, C., Li, Z., Penna, N. T., & Crippa, P. (2018). Generic atmospheric correction model for interferometric synthetic aperture radar observations. *Journal of Geophysical Research: Solid Earth*, *123*(10), 9202–9222. https://doi.org/10.1029/2017JB015305